

# Wing Noise Simulation of Supersonic Business Jet in Landing Configuration

Alexey P. Duben<sup>1</sup> , Tatiana K. Kozubskaya<sup>1</sup> , Pavel V. Rodionov<sup>1</sup> 

© The Authors 2024. This paper is published with open access at SuperFri.org

The paper presents the results of wing noise simulations for the prototype of supersonic business jet in landing mode. The near-field airflow is modeled according to Delayed Detached Eddy Simulation approach. The finite-volume vertex-centered scheme with the low weight of upwind component is used for convective flux approximation. The noise at the far-field points is calculated by the Ffowcs Williams–Hawkings method. The noise spectra at the near-field points are presented, and the impact of local mesh resolution and numerical instability on the near-field acoustics is discussed. For the Ffowcs Williams–Hawkings method due to the features of the wing geometry and the resulting flow configuration, we used non-standard integration surfaces to reduce computational costs of the scale-resolving simulations. Additionally, we employed optimized mesh resolution on the integration surfaces to significantly reduce the disk space required for storing the data for far-field noise calculations. The tests performed for the near-field and far-field points demonstrated applicability of the proposed optimizations.

*Keywords:* computational fluid dynamics, aeroacoustics, airframe noise, turbulent flow, detached eddy simulation, mixed-element mesh, FWH method.

## Introduction

The first generation of supersonic civil aircraft is represented by two airliners: Tupolev Tu-144 developed in Soviet Union (produced in 1967–1983) and Concorde jointly developed by France and United Kingdom (produced in 1965–1979). Despite considerable scientific and industry expectations, the level of technologies and materials available at the time did not allow such planes to become widely used and economically feasible. The main reason was the intractable problem of sonic boom. When an aircraft travels at speeds greater than the local speed of sound, it generates a number of shockwaves that transform to a short intense acoustic disturbance at long distances perceived as an explosion or a thunderclap near the ground surface. For civil aircrafts, this effect led to a temporary prohibition of supersonic flights over populated areas which made manufacturing and maintaining costs of supersonic airliners unreasonable.

Technological advances of the last fifty years, characterized by development of new materials, evolution of aircraft engines, progress in computer-aided engineering based on numerical modeling, improvement of automated systems for diagnostics and control, provoke attempts to design supersonic transport of a new generation. The primary focus of the corresponding projects that exist in Russia and in some other countries is to develop a supersonic business jet (SSBJ) for a small number of passengers that can provide low intensity of sonic boom at supersonic cruise flight [20]. Important technical tasks also include optimization of airframe aerodynamics for all flight modes, achievement of high fuel efficiency and reduction of total noisiness. According to preliminary technological and economical assessments [20], the supersonic business transport of a new generation will be able to provide high level of passenger safety and sufficient comfort of the flight while remaining commercially reasonable.

As for other civil aircrafts, SSBJ is required to comply with the current certification standards of International Civil Aviation Organization (ICAO) for noise during takeoff, flyover and approach to receive the permission to land at most airports. For modern commercial airliners,

---

<sup>1</sup>Keldysh Institute of Applied Mathematics, RAS, Moscow, Russian Federation

the dominant component to the total noise during takeoff is generated by engine [23]. During landing, the noise sources associated with engine (primarily with fan and turbine) also make a significant contribution to the total noise, however, the high bypass ratio of modern civil aircraft engines led to a comparable importance of the noise generated by airframe elements such as landing gear, slats and flaps [5, 6, 23]. For SSBJ, engine and jet will probably be the dominant noise sources at both takeoff and landing due to the reduced engine bypass ratio and the wing design features. To provide data supporting this hypothesis, we aimed to investigate the SSBJ wing noisiness in landing mode by numerical simulations. The final confirmation of this hypothesis is possible only after corresponding numerical and/or experimental studies of SSBJ landing gear and engine which are out of scope of this paper.

We present the results of scale-resolving wing noise simulations of SSBJ prototype in landing mode based on Delayed Detached Eddy Simulation (DDES) approach [12, 17]. Recently, wing noise simulation of other SSBJ prototype in landing mode was performed by NASA in collaboration with Dassault Systmes using the PowerFLOW code [7, 11, 14] based on lattice Boltzmann method (LBM).

## 1. Problem Formulation

The full-scale SSBJ airframe with  $10^\circ - 10^\circ$  deflection of droop noises and  $10^\circ - 20^\circ - 20^\circ - 10^\circ$  deflection of elevons on each side of the wing (Fig. 1) is placed inside the uniform airflow with the velocity  $U_\infty = 68$  m/s, the pressure  $P_\infty = 101325$  Pa and the temperature  $T_\infty = 288.15$  K at an angle of attack  $10^\circ$ . The length of considered geometry is 45 m, the wingspan is 20 m. The corresponding Mach number is 0.2, the Reynolds number based on the characteristic length  $L = 1$  m is  $4.6 \times 10^6$ .

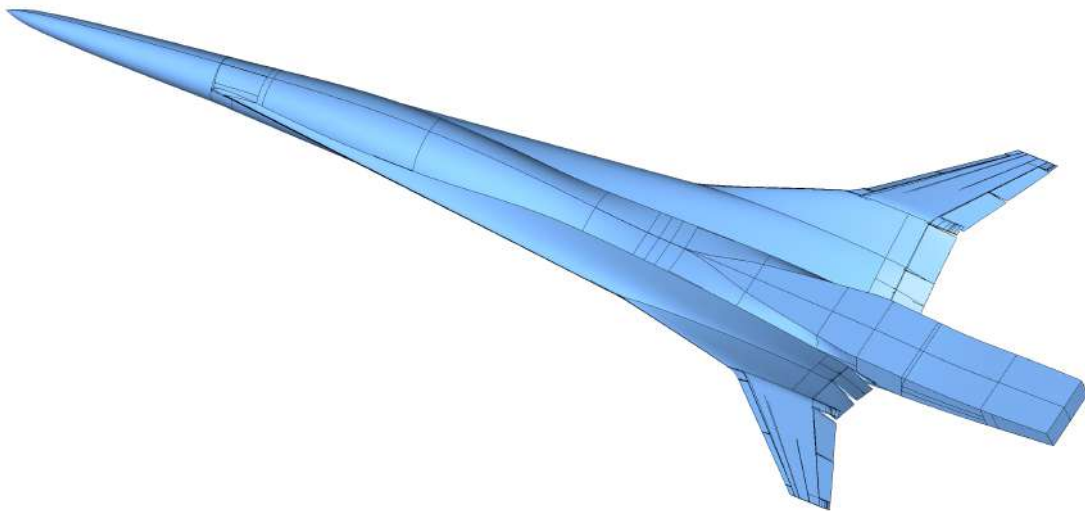


**Figure 1.** SSBJ airframe with high-lift devices in landing configuration

## 2. Computational Setup

To model the properties of air, we use the calorically perfect gas with the ratio of specific heats  $\gamma = 1.4$  and the specific gas constant  $R_{sp} = 287.05$  J/(kg K). For preliminary analysis of the flow, we perform simulations based on solving unsteady Reynolds-averaged Navier–Stokes

(RANS) equations with the Menter SST turbulence model adjusted by rotation and curvature correction of Stabnikov and Garbaruk [19]. We perform scale-resolving simulations according to the DDES approach [12, 17] with the subgrid scale  $\Delta = \tilde{\Delta}_\omega$  [12] and the subgrid model  $\sigma$  [13] in the large eddy simulation (LES) region and the Spalart–Allmaras (SA) turbulence model [18] in the RANS region.

Due to the symmetry of the considered geometry and the problem parameters, we simulate the flow only for half of the airframe. For visualization purposes, we duplicate and reflect the resulting flow fields relative to the plane of symmetry  $y = 0$ . All the acoustic data presented in the paper is calculated only for half of the airframe as well. Because the acoustic sources located on different sides of the airframe are spatially separated, we can consider them as uncorrelated. Hence, to obtain sound intensity for the full airframe, one can increase the corresponding intensity for half of the geometry by 3 dB.

The slip boundary conditions are set at the plane of symmetry  $y = 0$ , the free-stream conditions are used at the outer boundaries. Zero velocity and zero heat flux are specified on the streamlined geometry. To prevent the reflection of acoustic waves from the plane of symmetry in DDES simulations, the sponge layer [9] based on the averaged RANS solution is set in the region  $0 \text{ m} \leq z \leq 1.5 \text{ m}$ .

The computational domain is defined by the parallelepiped  $2000 \text{ m} \times 2000 \text{ m} \times 1000 \text{ m}$  with the exclusion of SSBJ airframe interior. The center of the boundary at the plane of symmetry is coincided with the reference point for pitching moment calculation located 31.5 m away from the SSBJ fore point along the  $x$ -axis.

We use the finite-volume vertex-centered EBR5 PL scheme [4] to approximate the convective flux and the method of local element splittings [3] to approximate the diffusive flux. For time integration, we apply the first-order implicit scheme based on the backward differentiation formula (BDF1) in RANS simulations and the second-order implicit BDF2 scheme in DDES simulations. To solve the system of nonlinear equations at each time step, we use one Newton iteration in RANS simulations and two Newton iterations in DDES simulations. At each iteration, we solve of the system of linear equations by the bi-conjugate gradient stabilized (BiCGStab) method [22] with the symmetric Gauss–Seidel (SGS) preconditioner.

Simulations are performed on two meshes denoted as Level A and Level B. Their general structure is shown in Fig. 2, their parameters are summarized in Tab. 1, where  $h_{\text{fuselage}}$  is the length of mesh edges in tangential directions near the fuselage and the lower surface of the wing,  $h_{\text{vortices}}$  is the length of mesh edges in the region of stable vortex flow over the wing. Outside the prismatic layers built near the streamlined geometry, the zone of increased mesh resolution over the wing is filled with an isotropic unstructured tetrahedral mesh.

**Table 1.** Mesh parameters

Mesh	$N_{\text{nodes}}$	$N_{\text{elements}}$	$N_{\text{surf.nodes}}$	$N_{\text{surf.elements}}$	$h_{\text{fuselage}}$	$h_{\text{vortices}}$
Level A	21 166 948	46 552 132	337 330	342 475	70 mm	35 mm
Level B	61 601 940	219 587 977	678 233	687 362	70 mm	17.5 mm

In RANS simulations, we use the maximum time step providing stability of the computational process. After reaching the steady state, the numerical solution is averaged over time interval 50–150  $L/U_\infty$  to obtain the resulting flow fields.

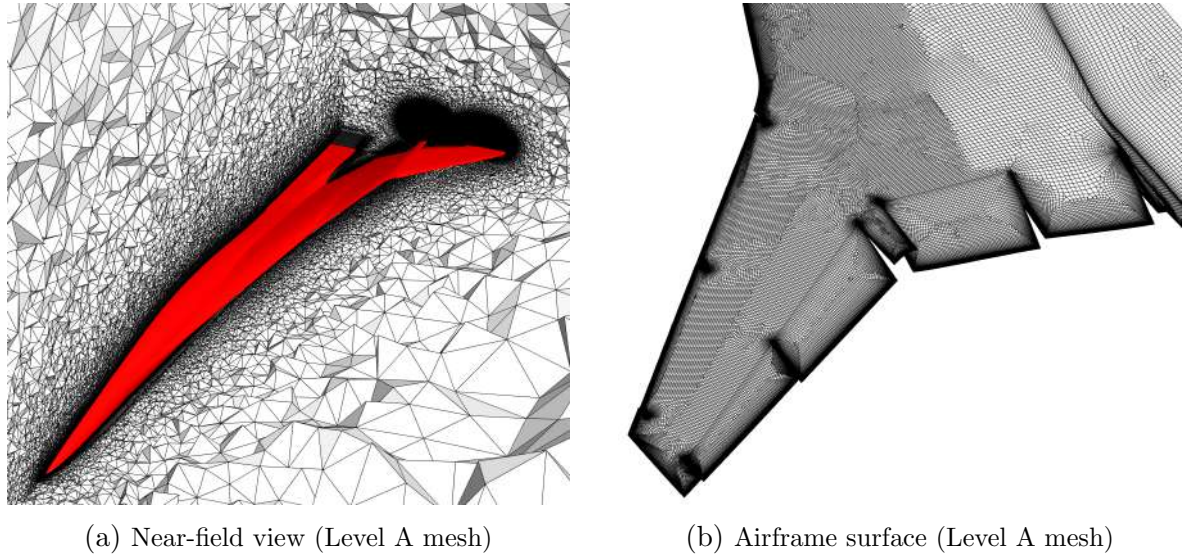


**Figure 2.** General mesh structure

In DDES simulations, we decrease the weight of upwind component of the EBR5 PL scheme according to the approach proposed in [10]. The minimum weight of upwind component in the zone of increased mesh resolution over the wing is set to 0.15. We choose the time step providing the relatively small size of regions containing numerical instability. In terms of  $CFL_{\text{vortices}} = \Delta t \times (c_\infty + U_\infty) / h_{\text{vortices}}$ , where  $\Delta t$  is the time step and  $c_\infty$  is the speed of sound at infinity, we use  $CFL_{\text{vortices}} = 0.083$  on the Level A mesh and  $CFL_{\text{vortices}} = 0.125$  on the Level B mesh. The initial flow fields for the DDES simulation on the Level A mesh are defined by the averaged RANS solution. The initial flow fields for the DDES simulation on the Level B mesh are defined by instantaneous DDES solution obtained on the Level A mesh after reaching the steady state according to aerodynamic coefficients. When the flow is reached the steady state and the instantaneous solution is proved to have only small regions of numerical instability, we start to record the near-field acoustic data and accumulate the average flow fields. The data recording is performed for time interval  $60 L/U_\infty$  or 0.88 s. This interval size allows us to obtain smoothed spectra (averaged for 30 time segments with 0.5 overlapping) at the near-field and far-field points with the minimum resolved frequency 20 Hz.

To evaluate the acoustic characteristics of the flow in the near field, pressure pulsations are recorded at the points of the discretized curves shown in Fig. 3. The approximate distance between these points is 10 cm, some of these points are marked with numerical labels. The lower curve is located approximately 4 cm below the wing edge, the upper curves are located approximately above the centers of the main vortices formed over the wing.

The second-order Ffowcs Williams–Hawkings (FWH) method [2, 8, 15, 16] was used to calculate acoustic pressure pulsations in the far field. The corresponding FWH surface with five end caps used for accumulation of the required acoustic data is located near the boundaries of the zone of increased mesh resolution (Fig. 4). Note that this surface has a slit on the fuselage side to prevent intersection with the wing surface. Formally, a non-closed surface is not allowed to be used for the FWH method, however, the construction of a closed surface for the considering problem is undesired for the following reasons.

If we locate the FWH surface at a significant distance from the SSBJ airframe, as it was done, for example, in [11, 14], the requirement to resolve acoustic pulsations on this surface will

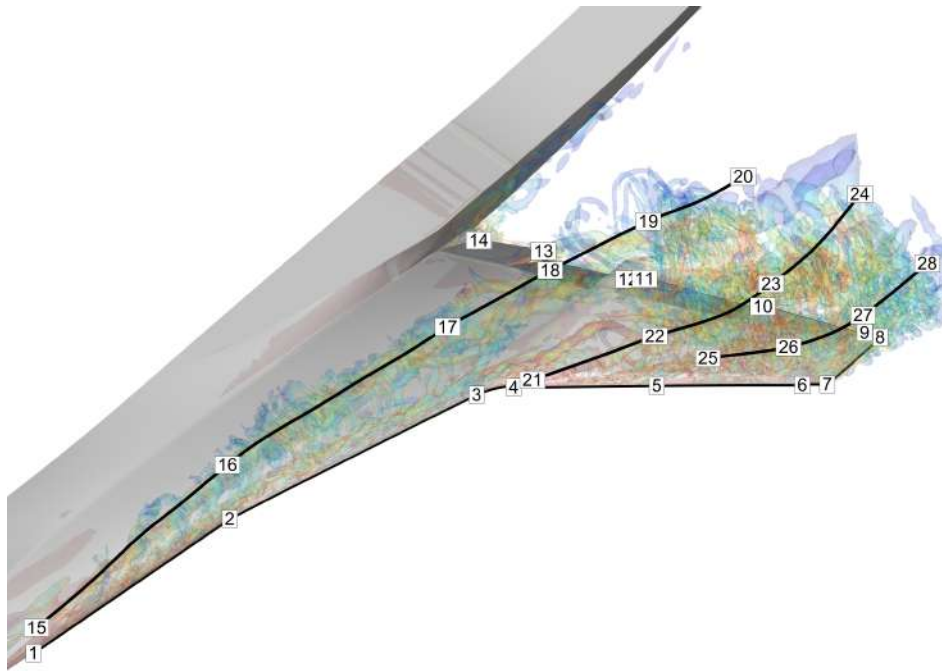


**Figure 3.** Location of pressure sensors in the near field

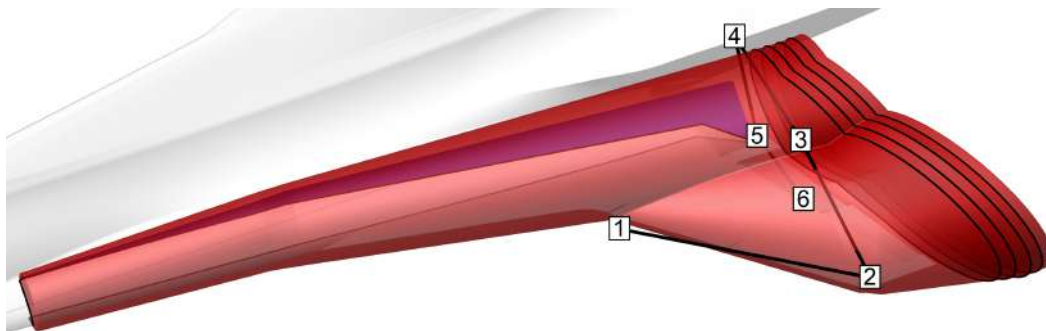


**Figure 4.** Location of FWH surface and the near-field points used to test FWH method

lead to the use of increased mesh resolution in the vicinity of the entire SSBJ airframe, resulting in a significant increase of computational cost of scale-resolving modeling. This approach would be rational if substantial acoustic sources are located along entire streamlined body. However, in the considered problem, the fuselage generates almost no large-scale turbulent pulsations that have any substantial effect on the total airframe noise.

In theory, one could propose to use a closed FWH surface formed by the union of the surface shown in Fig. 4 with some surface located in a slight distance from the streamlined geometry and containing the fuselage and wing root within. However, since the mesh resolution near the fuselage and wing root is coarser than the resolution inside the zone of intense vortical flow, acoustic perturbations propagating from the main vortices toward the plane of symmetry will rapidly dissipate, and hence their contribution to the far-field noise obtained by the FWH method will be close to zero. The use of increased mesh resolution near the fuselage and wing root will lead to unjustified increase of computational cost similar to the previous variant.

The main problem originating from the location of the FWH surface according to Fig. 4 is the inability to model the reflection of acoustic waves from the wing surface by the FWH method.

In scale-resolving simulation, acoustic waves propagating downward near the upper surface of the wing will be reflected. However, in calculation according to the FWH method, these waves will propagate to the region below the wing without any reflection. In order to evaluate the influence of the described effect on the far-field noise, the constructed surface was divided into two parts: the main surface denoted in Fig. 4 by red color, and the extension denoted in Fig. 4 by blue color. Further, we will use the label FWH to denote noise calculations based on the data from the main surface only, and the label FWH Ext to denote noise calculations based on the data from both the main surface and the extension. Note that all end caps (e.c.) belong to the main surface.

To find optimal mesh resolution for the FWH surface, we accumulate the required acoustic data on the three types of meshes formed mainly by quadrilaterals. We will use the label Coarse for isotropic meshes with edge length  $2h_{\text{vortices}}$ , the label Fine for isotropic meshes with edge length  $h_{\text{vortices}}$ , and the label Mixed for meshes with edge length  $h_{\text{vortices}}$  at end caps and edge length  $2h_{\text{vortices}}$  at the rest part of the FWH surface. We record the data with the sampling frequency  $(c_{\infty} + U_{\infty})/(2h_{\text{vortices}})$  on Coarse and Mixed meshes, and with the sampling frequency  $(c_{\infty} + U_{\infty})/h_{\text{vortices}}$  on Fine meshes.

The described methodology of noise calculation based on the FWH method is tested by comparing the acoustic spectra obtained by DDES simulations and FWH calculations at the near-field points. These points are located in the outer region relative to the FWH surface and denoted by numerical labels in Fig. 4. The far-field points used for SSBJ wing noise assessment (Fig. 5) belong to the sphere of radius 150 m.

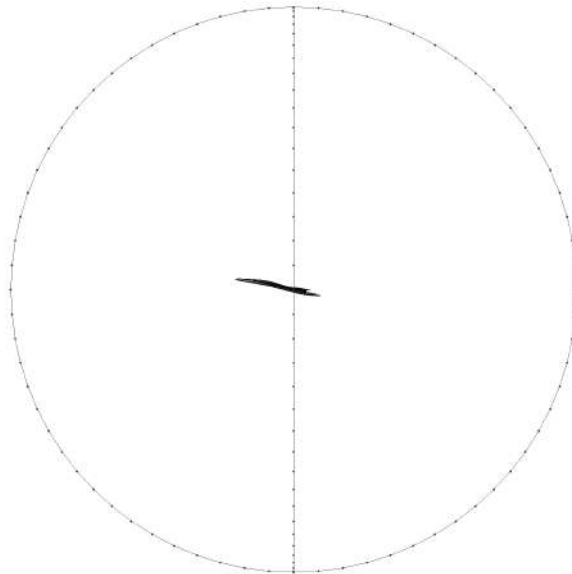


**Figure 5.** Location of the far-field points

All the simulations presented in this paper are performed using the NOISEtte code [1] written in C++ and suitable for computations in CPU, GPU (OpenCL) and heterogeneous CPU+GPU modes with combined MPI+OpenMP parallelization. DDES simulations are carried out using NVIDIA Tesla V100 GPUs on the Lomonosov-2 supercomputer [21] installed at Lomonosov Moscow State University. For the DDES simulation on the Level A mesh, 8 GPUs (4 compute nodes each equipped with 2 GPUs) are utilized for 21 hours to accumulate the required data on the time interval  $60 L/U_{\infty}$ . For the DDES simulation on the Level B mesh,

24 GPUs (12 compute nodes) are utilized for 24 hours to achieve the steady flow state and for 72 hours to accumulate the required data on the time interval  $60 L/U_\infty$ .

### 3. DDES Performance

For reliable flow modeling using the hybrid RANS-LES approach DDES, boundary layer should be simulated in RANS mode because mesh for DDES simulation is not fine enough in tangential direction near walls to resolve boundary layer in LES mode properly. The switching between RANS and LES modes in DDES is controlled by the  $f_d$  blending function.

DDES performance in the simulation of the flow around SSBJ airframe on the Level B mesh can be evaluated from Fig. 6 and Fig. 7. Isolines  $f_d = 0.99$  indicating approximate interface between RANS and LES zones are depicted in Fig. 6d for the instantaneous DDES solution (location of the corresponding cross sections is shown in Fig. 6a and Fig. 6b). Figure 6c presents isolines  $F_1 = 0.99$  of the SST  $F_1$  blending function for the averaged RANS solution. These isolines approximately correspond to the edge of boundary layer. Distributions of the distance to the wall  $d_w$  for the considered isolines as functions of the spanwise coordinate are shown in Fig. 6e for Section 1 and in Fig. 6f for Section 2. In most of the domain, the approximate interface between RANS and LES zones ( $f_d = 0.99$ ) lies farther from the wall than isosurface  $F_1 = 0.99$ , hence the boundary layer is simulated predominantly in RANS mode by DDES. Distributions of the friction coefficient  $C_f$  for the considered cross sections (Fig. 7) demonstrate that, except the regions with resolved turbulence, the averaged DDES solution is close to the averaged RANS solution, even though in the corresponding simulations the different turbulence models are used (SA in DDES and SST in RANS). Figure 6b shows the instantaneous distribution of the ratio between the subgrid scale  $\Delta$  and the distance to the wall  $d_w$  on isosurface  $f_d = 0.99$ . In the regions with no resolved turbulence, this ratio is mostly close to 1, while in the areas with stable vortical flow above the wing, where mesh resolution is intentionally better, it generally belongs to the interval  $0.2 \lesssim \Delta/d_w \lesssim 0.6$ .

Thus, we can conclude that the boundary layer shielding, in the sense of protecting boundary layer from switching to the unresolved LES regime, is effective and sufficient in the considered DDES simulation.

### 4. Aerodynamics

The mean flow fields obtained by DDES simulations are shown in Fig. 8. We see that the stable macro-scale vortices are formed over the wing at the considered angle of attack. These vortices provide a substantial region of rarefaction on the upper surface of the wing, which increases the airframe lift force. Despite some insignificant differences, the mean flows obtained on the Level A and Level B meshes are very close.

The values of aerodynamic coefficients obtained by RANS and DDES simulations on different meshes are given in Tab. 2. We see that the difference between the results of RANS and DDES simulations is approximately 3% in the lift coefficient, approximately 5% in the drag coefficient, and 10–15% in the pitching moment coefficient. We also note that mesh refinement slightly increases the difference between the RANS and DDES solutions in lift and pitching moment coefficients while the difference in drag coefficient remains almost unchanged.

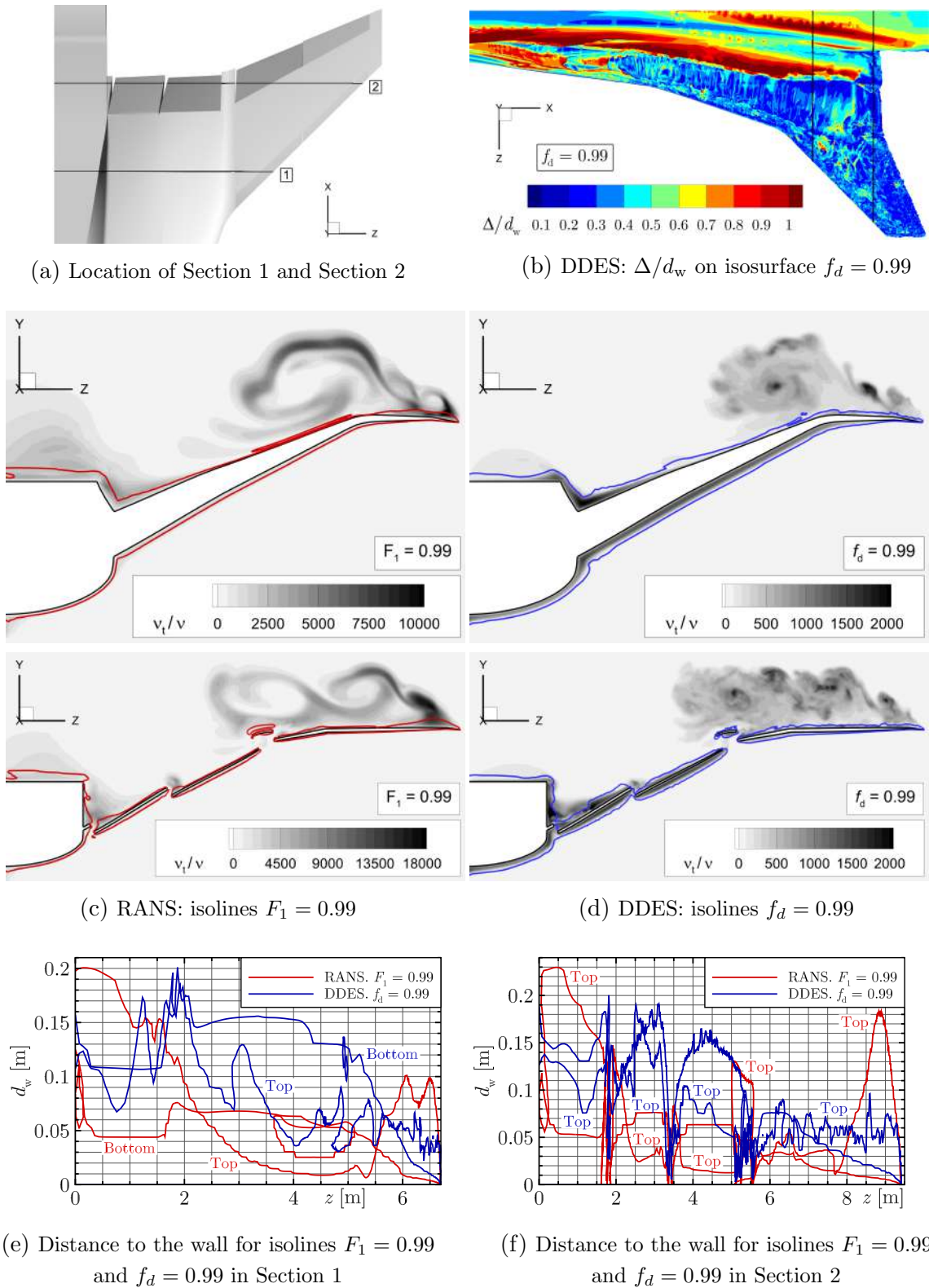


**Figure 6.** Boundary layer thickness: averaged RANS and instantaneous DDES solutions on the Level B mesh ( $\Delta$  is the subgrid scale,  $d_w$  is the distance to the wall,  $F_1$  is the SST blending function,  $f_d$  is the DDES blending function;  $\nu$  is the kinematic viscosity,  $\nu_t$  is the kinematic turbulent viscosity)

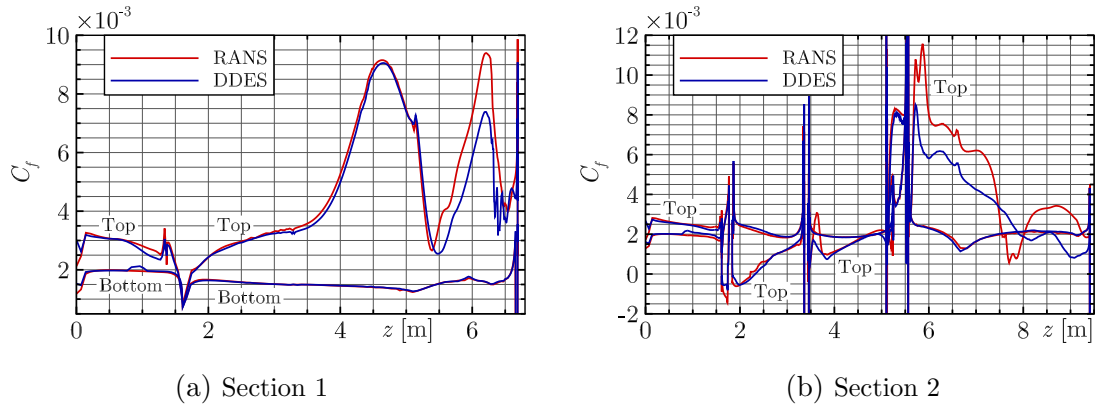


Figure 7. Skin friction coefficient: averaged RANS and averaged DDES solutions

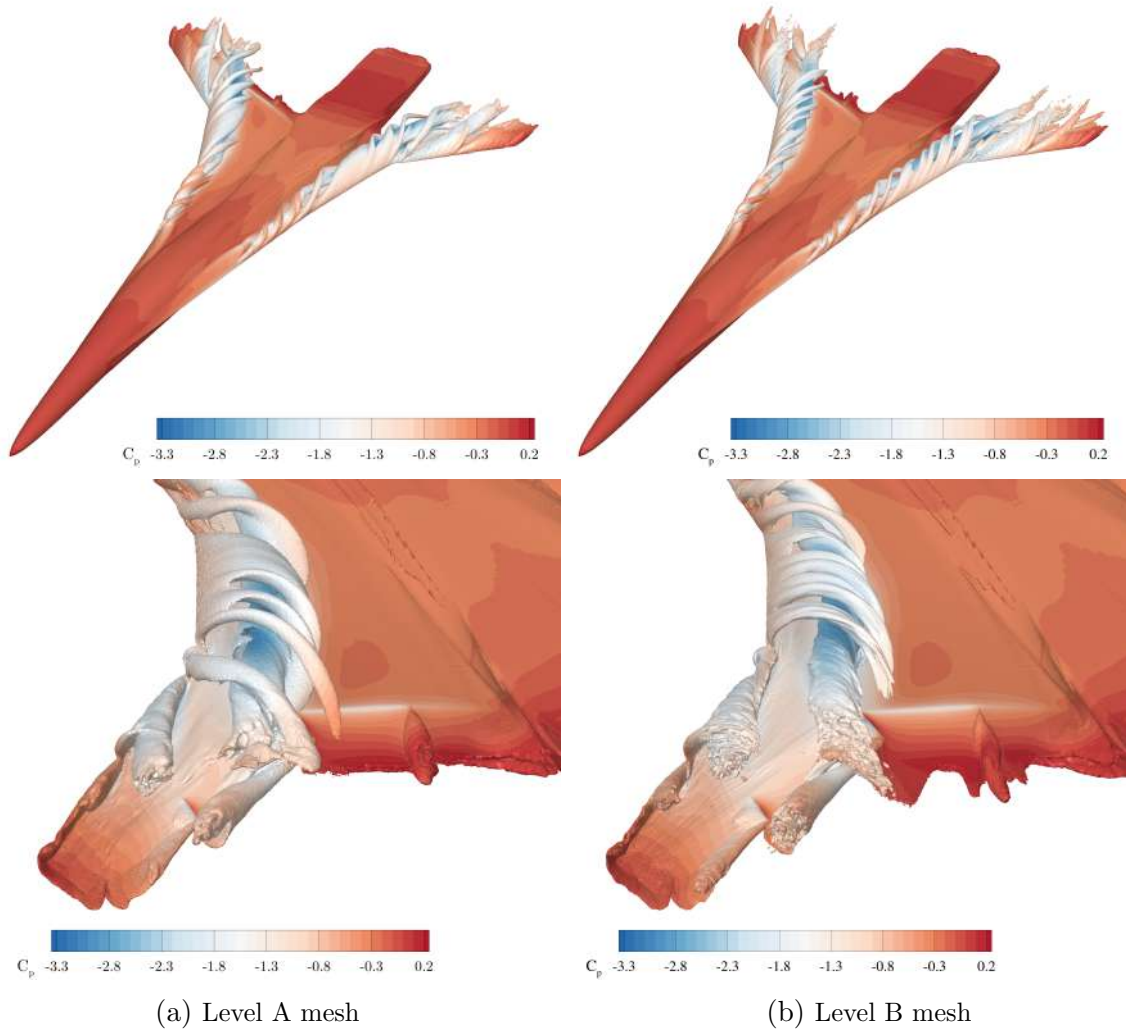


Figure 8. Mean flow fields obtained by DDES simulations (isosurfaces of vorticity magnitude corresponding to the value 200 1/s colored by pressure coefficient)

**Table 2.** Lift (CL), drag (CD) and pitching moment (CM) coefficients

	CL	diff	%	CD	diff	%	CM	diff	%
RANS (Level A)	0.907	0.025	2.9%	0.2244	0.0102	4.8%	-0.0638	-0.0060	10.3%
RANS (Level B)	0.914	0.032	3.7%	0.2255	0.0113	5.3%	-0.0677	-0.0099	17.1%
DDES (Level A)	0.878	-0.004	0.4%	0.2132	-0.0010	0.5%	-0.0566	0.0013	2.2%
DDES (Level B)	0.881	0	0.0%	0.2142	0	0.0%	-0.0578	0	0.0%

## 5. Near-Field Acoustics

The instantaneous flow fields obtained by DDES simulations after reaching the steady state are shown in Fig. 9. We see that the turbulent vortical flow over the wing surface is a source of acoustic pulsations. In the vicinity of the fuselage, the flow is almost stationary and does not contain significant acoustic sources. As it was expected, the mesh refinement allow DDES method to reproduce smaller turbulent structures above the wing, which leads to the appearance of higher-frequency harmonics in the simulated noise. Outside the zone of increased mesh resolution over the wing, acoustic pulsations rapidly dissipate due to increasing size of mesh edges.

The noise spectra at points of the near-field curves (Fig. 3) are shown in Fig. 10. We see that the presented spectra are more broadband near the geometry corners of the wing and its high-lift devices comparing to the rest of the computational domain. This effect is caused by a higher mesh resolution used for proper discretization of the corresponding geometry features. The resulting high-frequency components of the noise can be of a pure numerical nature or even related to numerical instability since a much coarser mesh is used at the rest of the domain. As we move along the wing edge toward the wing tip, the spectra shift almost linearly toward the low frequencies. This feature can be explained by the gradual enlargement of the stable vortices formed over the wing, which are the main sources of the wing noise. At the points close to the wing edge, the spectra contain narrowband peaks at high frequencies that appear to be very sensitive to the mesh resolution. These peaks are the footprints of the small local regions of numerical instability dependent on mesh and parameters of numerical method. On the curve located above the center of the main vortex, the numerical instability does not arise due to the relatively large size of the corresponding mesh elements. Hence, the spectra on this curve does not contain narrowband high-frequency peaks and sudden expansions in the resolved frequency range.

The acoustic spectra calculated for the near-field points marked with numerical labels (Fig. 3) are shown in Fig. 11. In accordance with the results presented in Fig. 10, these spectra are broadband, and, at most points, the intensity of noise decreases with increasing frequency. Similar features of noise spectra were obtained in [11, 14]. As location and size of regions containing numerical instability depend on mesh, the comparison of the spectra obtained by scale-resolving simulations on the Level A and Level B meshes allow us to evaluate the impact of numerical instability on the resulting flow acoustics. For example, when switching from the Level A mesh to the Level B mesh, the narrowband high-frequency peaks disappear from the spectra for points 11, 12, while such peaks arise in the spectra for points 5, 6, 10. Note that these narrowband peaks do not affect considerably the general features of the noise spectra in the near field.

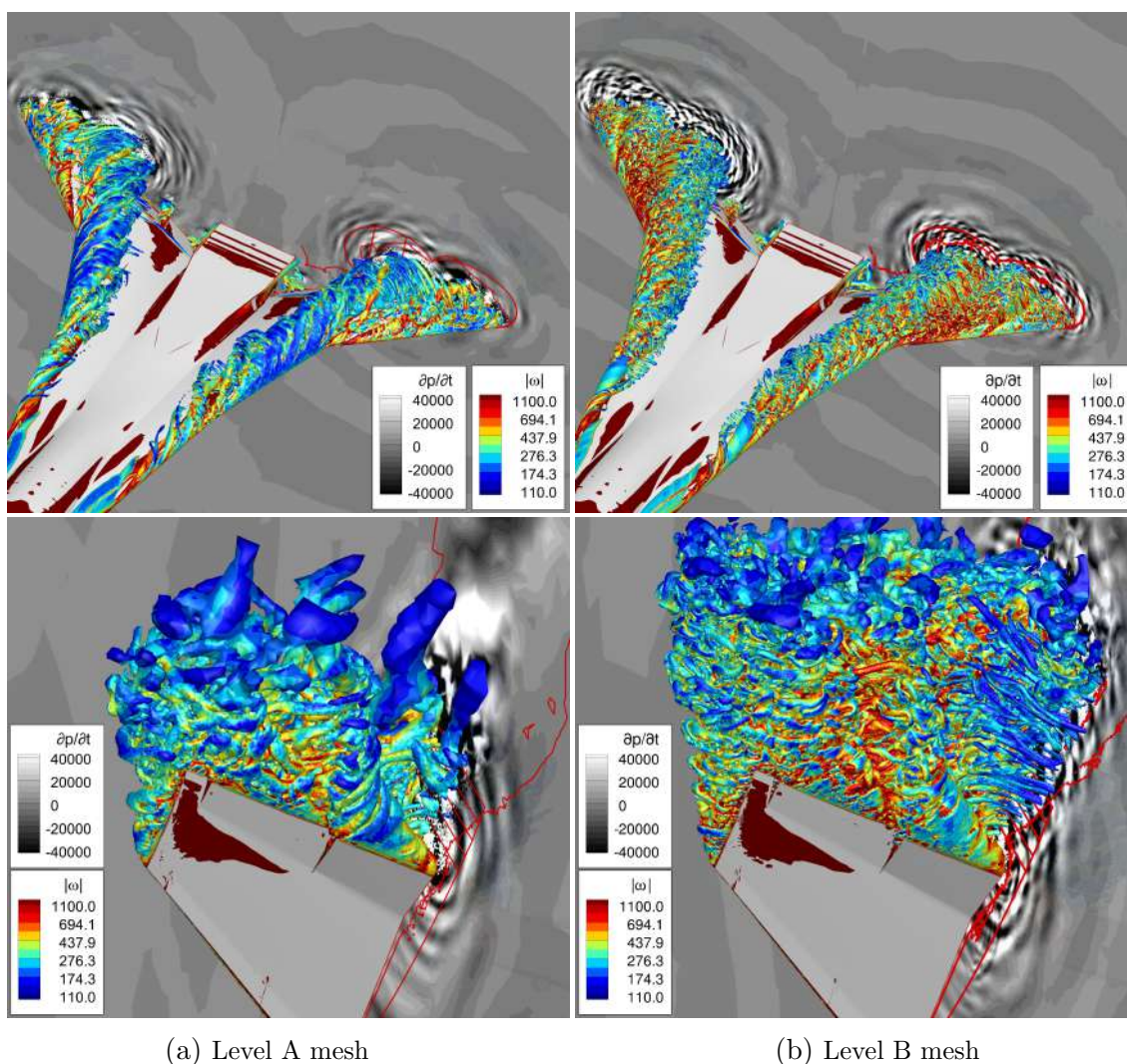


**Figure 9.** Instantaneous flow fields obtained by DDES simulations (time derivative of pressure and Q-criterion isosurfaces corresponding to the value  $5000 \text{ 1/s}^2$  colored by vorticity magnitude). The smooth curves denote position of the FWH surface, the non-smooth curves denote location of the isosurface of mean vorticity magnitude corresponding to the value  $2 \text{ 1/s}$

## 6. Far-Field Acoustics

To test the approach to far-field noise calculation described in Section 2, we compare the spectra based on pressure history extracted directly from the DDES solution and the spectra calculated using the FWH method at the near-field points marked with numerical labels in Fig. 4.

Comparison of noise spectra calculated using the Coarse and Fine FWH meshes is shown in Fig. 12. We see that for the Coarse FWH mesh the use of 5 end caps is preferable because the results for 3 end caps demonstrate an increase of error for some frequency bands by approximately 2 dB. For the Fine FWH mesh, there is almost no difference between the results obtained with 3 and 5 end caps. Note that the use of the Coarse FWH mesh is justified as the high-frequency range [5 kHz, 10 kHz] resolved by the Fine FWH mesh is not properly resolved in the DDES simulation. At the considered near-field points, the Coarse and Fine FWH meshes without end caps provide almost identical spectra, very close to the spectra based on pressure history. The spectra obtained using the Fine FWH mesh with 1 end cap are appeared to be

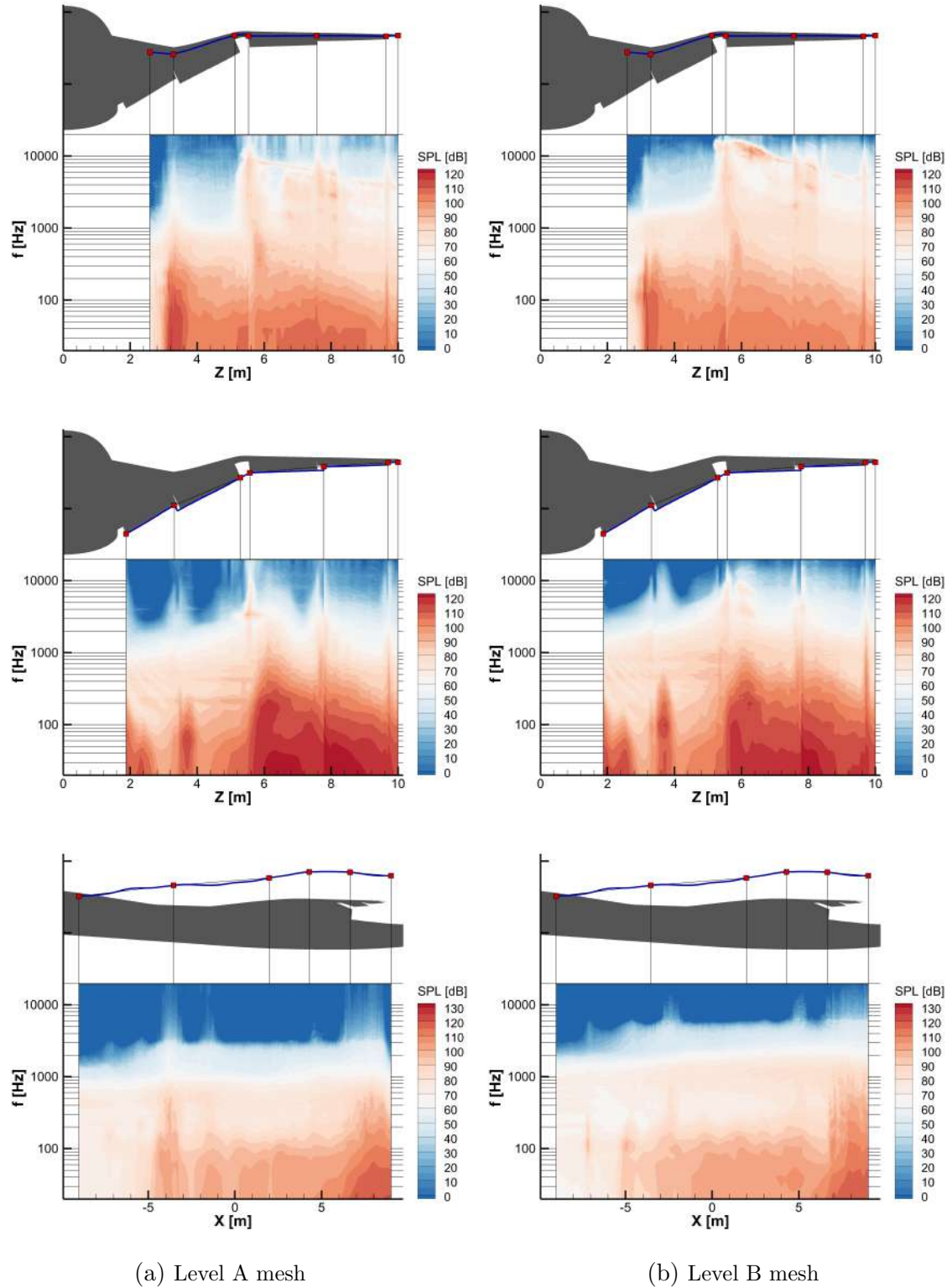


**Figure 10.** Noise spectra in the near field

more accurate than the spectra obtained using the Coarse FWH mesh with 1 end cap. Hence, to reduce the volume of accumulated data, one may replace the Fine FWH mesh by the Mixed FWH mesh (and use the sampling frequency corresponding to the Coarse FWH mesh) and receive almost the same results in the far field.

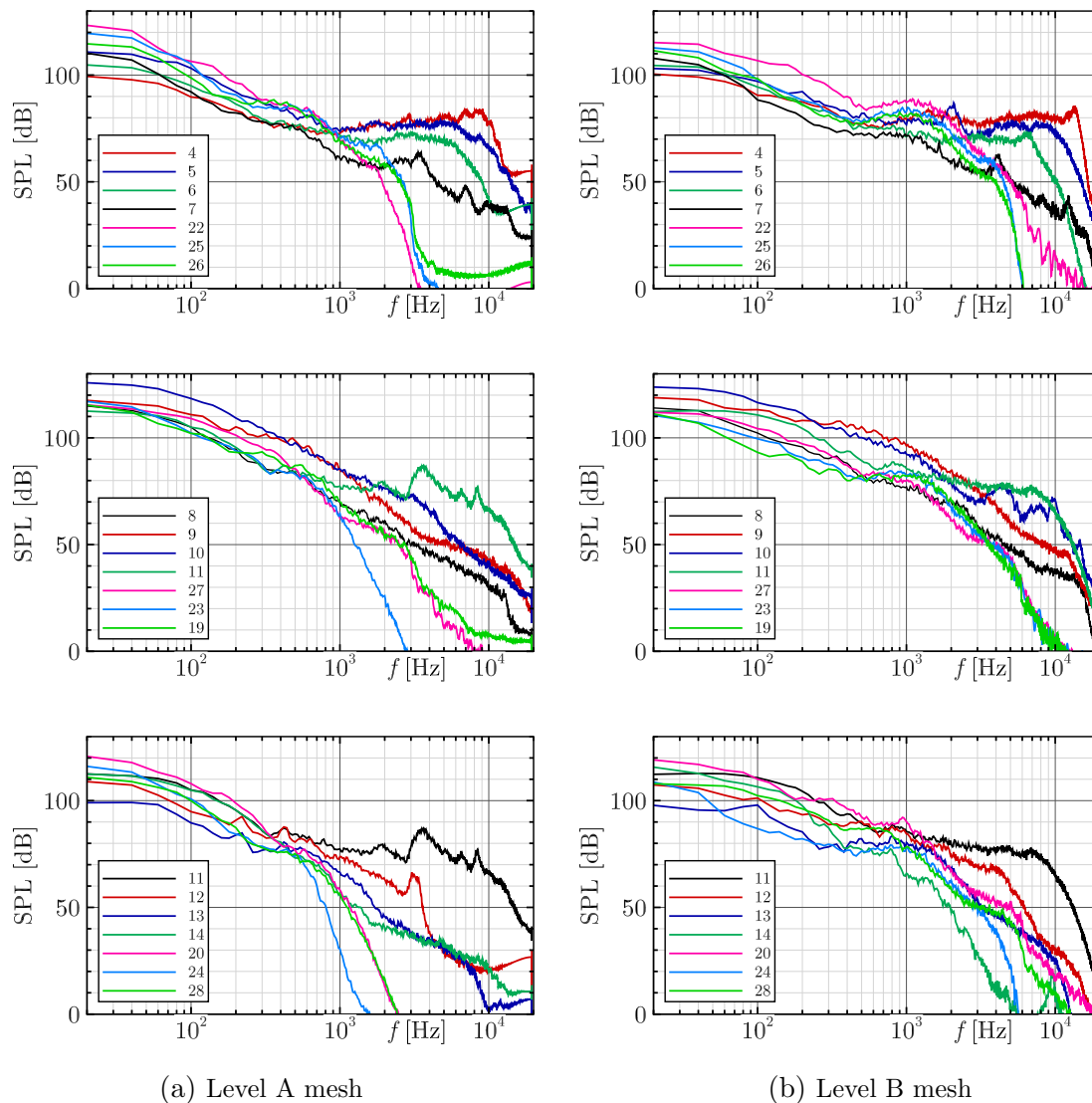
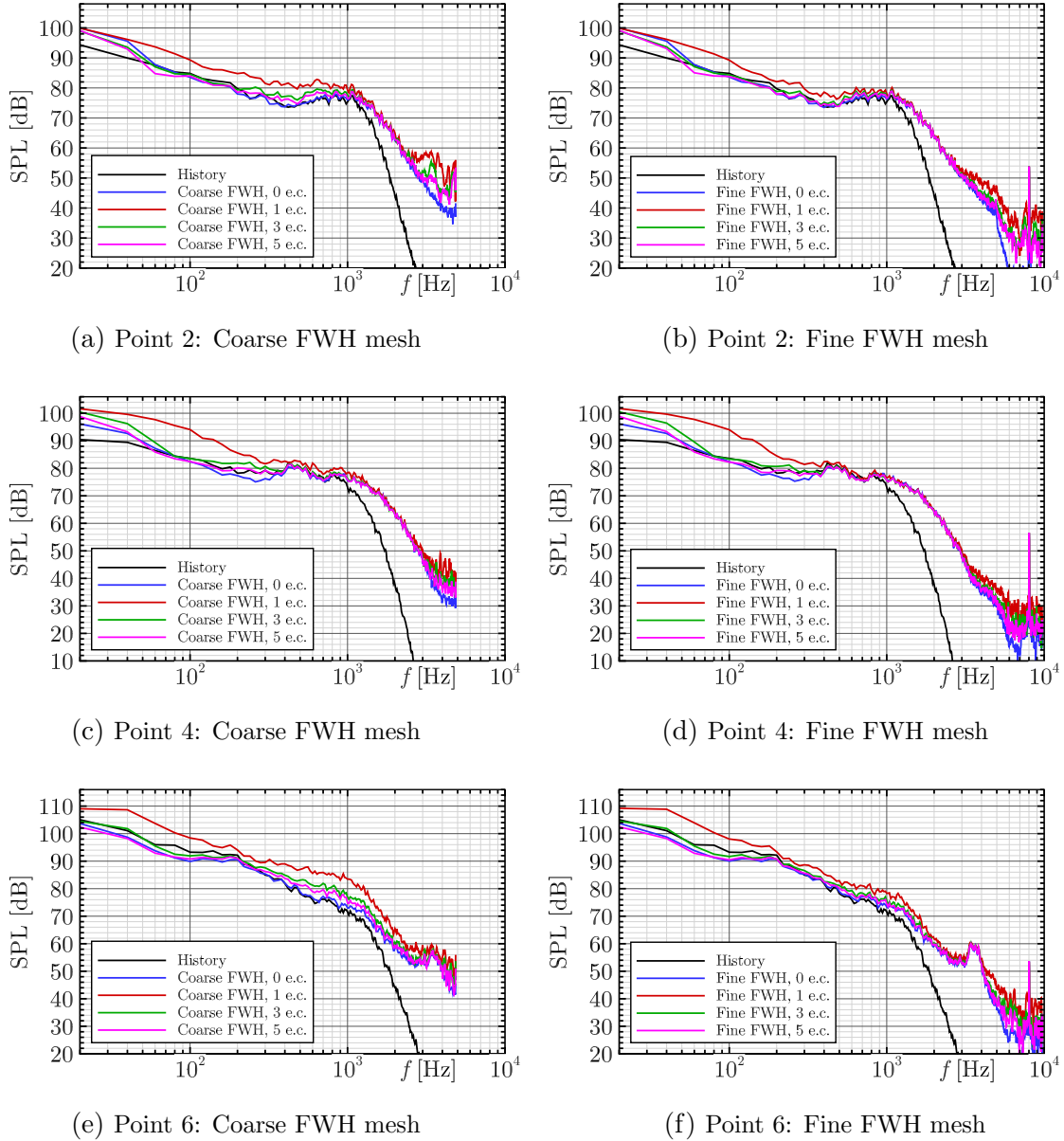


Figure 11. Noise spectra in the specific near-field points

For comparison of the FWH and FWH Ext surfaces, we choose the point closest to the FWH extension (Point 5 in Fig. 4). Figure 13 shows that the main difference between the basic and extended FWH surfaces appears in the range [40 Hz, 400 Hz]. We see that this difference is limited by 6 dB while the difference between the spectra calculated by the FWH method and the spectra based on pressure history in the range [40 Hz, 400 Hz] reaches 4–6 dB at some frequencies. At other test points, the difference between the basic and extended FWH surfaces is barely recognizable.

The spectra obtained by the FWH method at far-field points (Fig. 5) depending on the DDES and FWH meshes are presented in Fig. 14. We see that the spectra based on the data extracted from DDES simulations on the Level A and Level B meshes quantitatively differ by about 2.5 dB over a wide frequency range. The difference between the spectra calculated using the Coarse and Fine FWH meshes is less than 1 dB at most far-field points and frequency ranges.

Dependence of the far-field noise spectra on the use of the extended FWH surface is shown in Fig. 15. The main impact of the FWH extension is concentrated in the low-frequency range



**Figure 12.** Comparison of noise spectra extracted directly from the DDES solution (History) and calculated using the FWH method (Coarse FWH, Fine FWH). Raw numerical data is accumulated during the DDES simulation on the Level B mesh

[20 Hz, 100 Hz], where the difference between the FWH and FWH Ext surfaces can reach 2–5 dB. Figure 15 also presents the far-field noise spectra calculated using the Mixed FWH mesh. We see that the spectra obtained using the Mixed and Fine FWH meshes differ only at the high-frequency range, which is not properly resolved in the DDES simulation.

We note that the use of the Coarse FWH mesh instead of the Fine FWH mesh leads to an 8-fold reduction in disk space required for storing FWH data and a 2-fold reduction in the FWH sampling frequency in DDES simulation. For example, in DDES simulation on the Level B mesh, 523 GB and 72 GB of FWH data is accumulated for the Fine FWH mesh and for the Coarse FWH mesh, respectively. Because the corresponding impact on the spectra is within 1 dB, this approach is justified from a practical point of view. If higher accuracy is needed, one can use

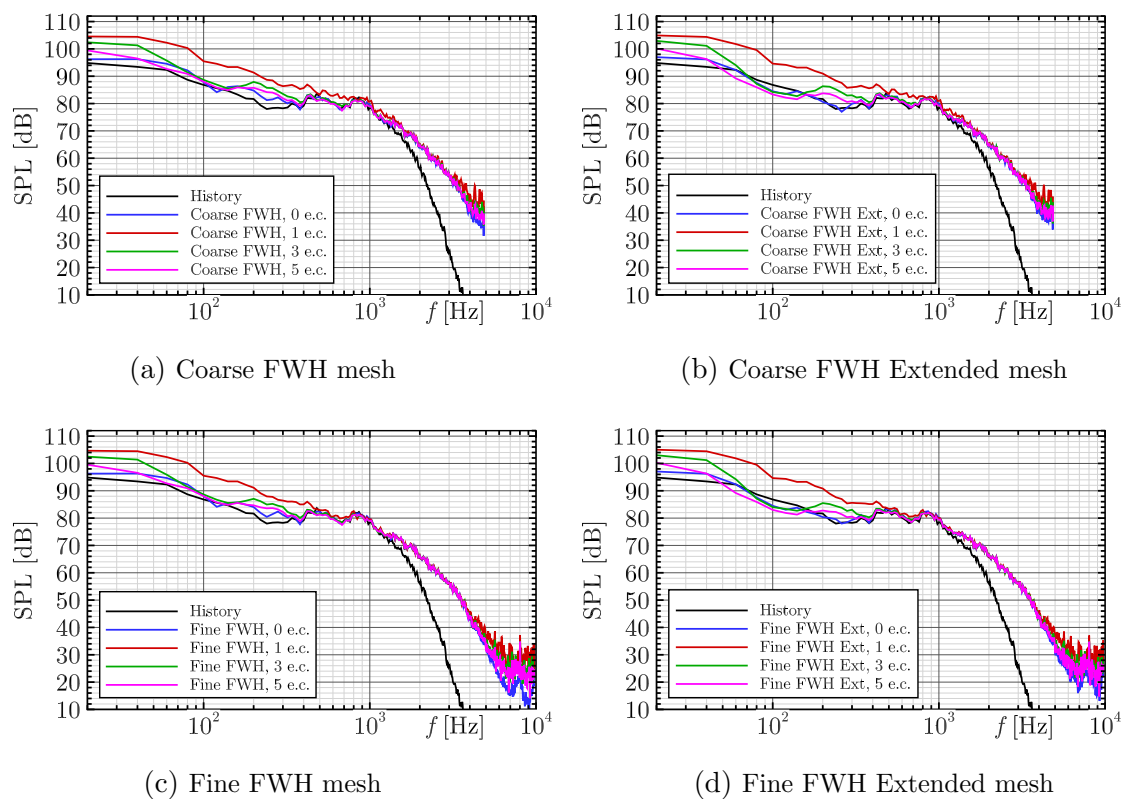


**Figure 13.** Comparison of noise spectra at Point 5 extracted directly from the DDES solution (History) and calculated using the FWH method. Raw numerical data is accumulated during the DDES simulation on the Level B mesh

the Mixed FWH mesh instead of the Fine FWH mesh. In DDES simulation on the Level B mesh, the Mixed FWH mesh provides a 3.3-fold reduction in disk space required for storing FWH data (158 GB of accumulated FWH data instead of 523 GB) along with a 2-fold reduction in the FWH sampling frequency. If the area of end caps is small relative to the area of entire FWH surface, the use of the Mixed FWH mesh instead of the Fine FWH mesh would lead to approximately an 8-fold reduction in the required disk space.

## Conclusions

The performed scale-resolving simulations of the wing noise for the supersonic business jet in landing configuration demonstrated the ability of hybrid RANS-LES methods to successfully solve the challenging aviation problems. The computations based on DDES approach allowed us to investigate aerodynamics of the target flow, accumulate and analyze the acoustic data in the near field, and calculate the far-field noise using the FWH method. The obtained results can be used for estimation of the total noise of supersonic business jets in landing mode for the international aircraft noise certification.

Particular attention in the presented study is paid for parameters of the FWH method. The considered wing geometry, the features of the target flow and the desire to reduce computational cost of DDES simulations provoked construction of the non-standard FWH surfaces. These surfaces were placed around the region of the intense vortical flow, but did not contain the

whole streamlined geometry within. The tests at the near-field and far-field points showed the applicability of the proposed surfaces for the FWH method. We also investigated the impact of the FWH surface discretization on properties of the calculated signals, and, finally, proposed the parameters of the mixed FWH mesh resolution that allows to save up to 8 times disk space required for storing FWH data.

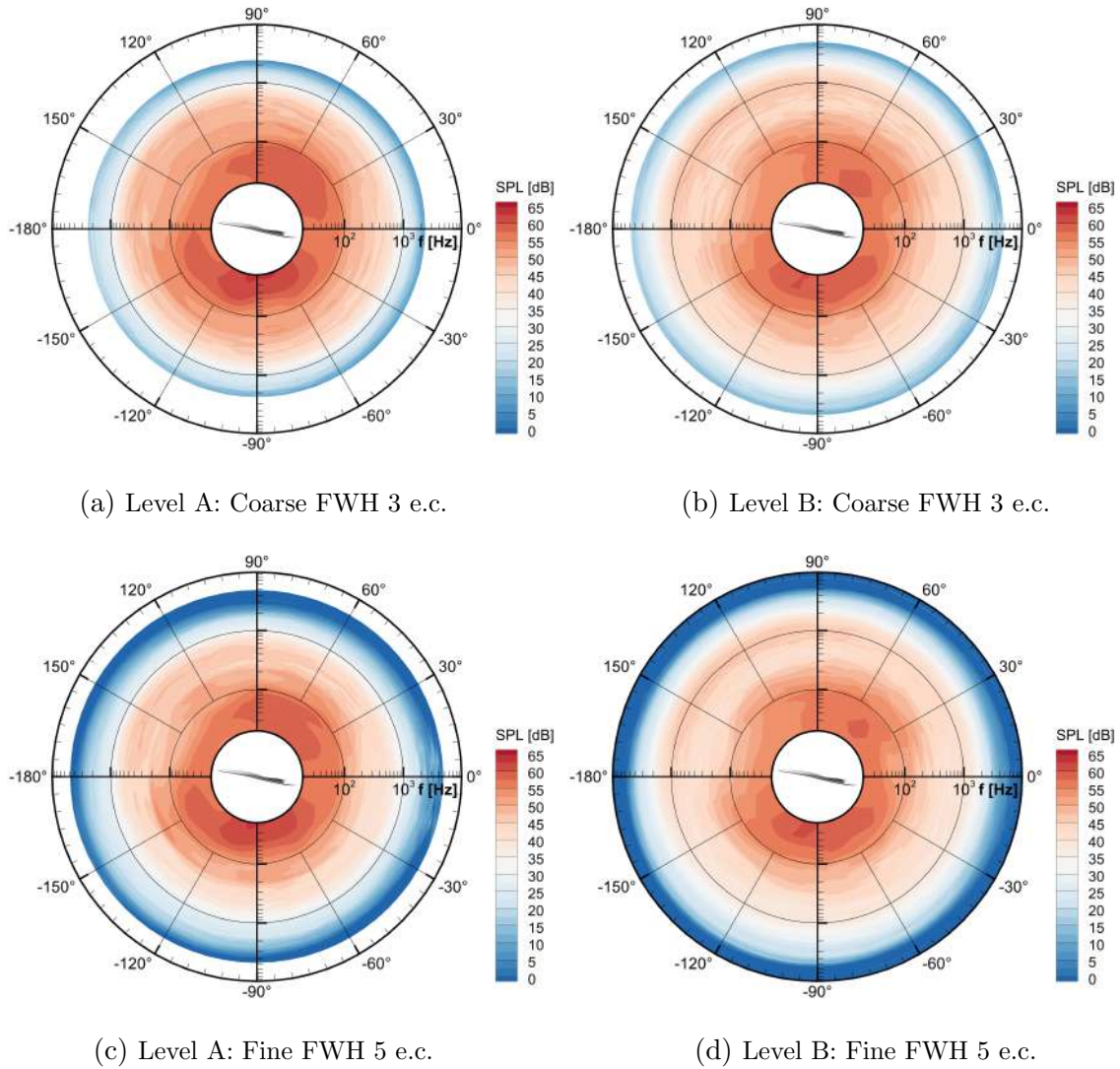


**Figure 14.** Noise spectra of the SSBJ wing in landing configuration at the far-field points. Raw numerical data is accumulated on the Coarse and Fine FWH surface meshes during DDES simulations on the Level A and Level B meshes

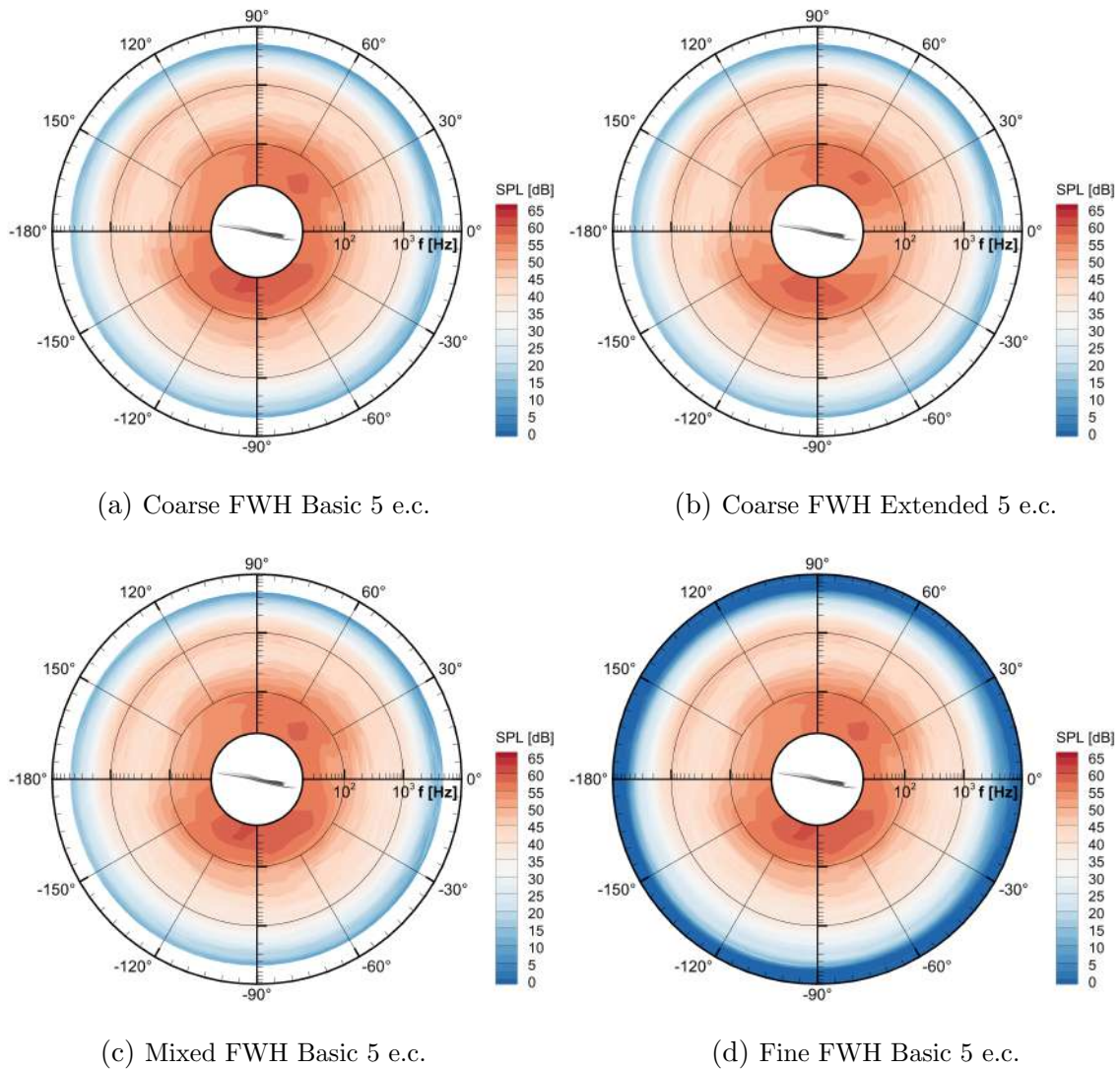


**Figure 15.** Noise spectra of the SSBJ wing in landing configuration at the far-field points. Raw numerical data is accumulated on the Coarse, Fine and Mixed FWH surface meshes during the DDES simulation on the Level B mesh

## Acknowledgements

The paper is prepared in the implementation of the program for the creation and development of the World-Class Research Center “Supersonic” for 2020–2025 funded by the Ministry of Science and Higher Education of the Russian Federation (Grant agreement of 25.04.2022, № 075-15-2022-330). The research is carried out using the equipment of the shared research facilities of HPC computing resources at Lomonosov Moscow State University with the additional use of the hybrid supercomputer K60 installed in the Supercomputer Centre of Collective Usage of KIAM RAS.

*This paper is distributed under the terms of the Creative Commons Attribution-Non Commercial 3.0 License which permits non-commercial use, reproduction and distribution of the work without further permission provided the original work is properly cited.*

## References

1. Abalakin, I.V., Bakhvalov, P.A., Bobkov, V.G., *et al.*: NOISEtte CFD&CAA Supercomputer Code for Research and Applications. *Supercomput. Front. Innov.* 11(2), 78–101 (aug 2024). <https://doi.org/10.14529/jsfi240206>
2. Bakhvalov, P.A., Kozubskaya, T.K., Kornilina, E.D., *et al.*: Technology of predicting acoustic turbulence in the far-field flow. *Math. Model. Comput. Simulations* 4(3), 363–373 (may 2012). <https://doi.org/10.1134/S2070048212030039>
3. Bakhvalov, P.A., Surnachev, M.D.: Method of averaged element splittings for diffusion terms discretization in vertex-centered framework. *J. Comput. Phys.* 450, 110819 (feb 2022). <https://doi.org/10.1016/J.JCP.2021.110819>
4. Bakhvalov, P., Kozubskaya, T., Rodionov, P.: EBR schemes with curvilinear reconstructions for hybrid meshes. *Comput. Fluids* 239, 105352 (may 2022). <https://doi.org/10.1016/J.COMPFLUID.2022.105352>
5. Delfs, J.: Simulation of aircraft installation noise – a key to low noise aircraft design (2016), [https://ceaa.imamod.ru/2016/files/ceaa2016.pdfs/D3S01\\_Delfs.pdf](https://ceaa.imamod.ru/2016/files/ceaa2016.pdfs/D3S01_Delfs.pdf)
6. Dobrzynski, W., Ewert, R., Pott-Pollenske, M., *et al.*: Research at DLR towards airframe noise prediction and reduction. *Aerosp. Sci. Technol.* 12(1), 80–90 (jan 2008). <https://doi.org/10.1016/j.ast.2007.10.014>
7. Ferris, R., Sacks, M., Cerizza, D., *et al.*: Aeroacoustic Computations of a Generic Low Boom Concept in Landing Configuration: Part 1 – Aerodynamic Simulations. *AIAA Aviat. Aeronaut. Forum Expo. AIAA Aviat. Forum 2021* (2021). <https://doi.org/10.2514/6.2021-2195>
8. Ffowcs Williams, J.E., Hawkings, D.L.: Sound generation by turbulence and surfaces in arbitrary motion. *Philos. Trans. R. Soc. London. Ser. A, Math. Phys. Sci.* 264(1151), 321–342 (may 1969). <https://doi.org/10.1098/rsta.1969.0031>
9. Gorobets, A.V., Duben, A.P., Kozubskaya, T.K., Rodionov, P.V.: Approaches to the Numerical Simulation of the Acoustic Field Generated by a Multi-Element Aircraft Wing in High-Lift Configuration. *Math. Model. Comput. Simulations* 15(1), 92–108 (feb 2023). <https://doi.org/10.1134/S2070048223010088>
10. Guseva, E.K., Garbaruk, A.V., Strelets, M.K.: An automatic hybrid numerical scheme for global RANS-LES approaches. *J. Phys. Conf. Ser.* 929(1), 012099 (nov 2017). <https://doi.org/10.1088/1742-6596/929/1/012099>
11. Khorrami, M.R., Shea, P.R., Winski, C.S., *et al.*: Aeroacoustic Computations of a Generic Low Boom Concept in Landing Configuration: Part 3 – Aerodynamic Validation and Noise Source Identification. *AIAA Aviat. Aeronaut. Forum Expo. AIAA Aviat. Forum 2021* (2021). <https://doi.org/10.2514/6.2021-2197>
12. Mockett, C., Fuchs, M., Garbaruk, A., *et al.*: Two Non-zonal Approaches to Accelerate RANS to LES Transition of Free Shear Layers in DES. In: *Prog. Hybrid RANS-LES Model.*, vol. 130, pp. 187–201. Springer Verlag (2015). [https://doi.org/10.1007/978-3-319-15141-0\\_15](https://doi.org/10.1007/978-3-319-15141-0_15)

13. Nicoud, F., Toda, H.B., Cabrit, O., *et al.*: Using singular values to build a subgrid-scale model for large eddy simulations. *Phys. Fluids* 23(8), 085106 (aug 2011). <https://doi.org/10.1063/1.3623274>
14. Ribeiro, A.F., Ferris, R., Khorrami, M.R.: Aeroacoustic Computations of a Generic Low Boom Concept in Landing Configuration: Part 2 – Airframe Noise Simulations. *AIAA Aviat. Aeronaut. Forum Expo. AIAA Aviat. Forum 2021* (2021). <https://doi.org/10.2514/6.2021-2196>
15. Shur, M.L., Spalart, P.R., Strelets, M.K.: Noise Prediction for Increasingly Complex Jets. Part I: Methods and Tests. *Int. J. Aeroacoustics* 4(3), 213–245 (jul 2005). <https://doi.org/10.1260/1475472054771376>
16. Shur, M.L., Spalart, P.R., Strelets, M.K.: Noise Prediction for Increasingly Complex Jets. Part II: Applications. *Int. J. Aeroacoustics* 4(3), 247–266 (jul 2005). <https://doi.org/10.1260/1475472054771385>
17. Shur, M.L., Spalart, P.R., Strelets, M.K., Travin, A.K.: An Enhanced Version of DES with Rapid Transition from RANS to LES in Separated Flows. *Flow, Turbul. Combust.* 95(4), 709–737 (jun 2015). <https://doi.org/10.1007/S10494-015-9618-0>
18. Spalart, P.R., Allmaras, S.R.: A one-equation turbulence model for aerodynamic flows. In: *AIAA Pap.* 92-0439 (1992). <https://doi.org/10.2514/6.1992-439>
19. Stabnikov, A.S., Garbaruk, A.V.: Testing of modified curvature-rotation correction for  $k-\omega$  SST model. *J. Phys. Conf. Ser.* 769(1), 012087 (nov 2016). <https://doi.org/10.1088/1742-6596/769/1/012087>
20. Sun, Y., Smith, H.: Review and prospect of supersonic business jet design. *Prog. Aerosp. Sci.* 90, 12–38 (2017). <https://doi.org/10.1016/j.paerosci.2016.12.003>
21. Voevodin, V.V., Antonov, A.S., Nikitenko, D.A., *et al.*: Supercomputer Lomonosov-2: Large Scale, Deep Monitoring and Fine Analytics for the User Community. *Supercomput. Front. Innov.* 6(2), 4–11 (jun 2019). <https://doi.org/10.14529/jsfi190201>
22. van der Vorst, H.A.: Bi-CGSTAB: A Fast and Smoothly Converging Variant of Bi-CG for the Solution of Nonsymmetric Linear Systems. *SIAM J. Sci. Stat. Comput.* 13(2), 631–644 (1992). <https://doi.org/10.1137/0913035>
23. Zaporozhets, O., Tokarev, V.I., Attenborough, K.: *Aircraft Noise: Assessment, prediction and control.* Spon Press (2011), [https://books.google.com/books/about/Aircraft\\_Noise.html?hl=ru&id=wSMXnVVgOSQC](https://books.google.com/books/about/Aircraft_Noise.html?hl=ru&id=wSMXnVVgOSQC)